

1 **Investigation of the  $\text{NaNi}_x\text{Mn}_{1-x}\text{O}_2$  ( $0 \leq x \leq 1$ ) System for Na-ion Battery Cathode Materials**

2

3

R. Fielden and M.N. Obrovac\*

4

5

Department of Chemistry, Dalhousie University, Halifax, N.S., B3H 4R2 Canada

6

7

\* - corresponding author: mnobrovac@dal.ca

8

9

**Abstract**

10

Layered  $\text{NaNi}_x\text{Mn}_{1-x}\text{O}_2$  ( $0 \leq x \leq 1$ ) oxides were prepared via solid state reactions.

11

Different reaction conditions were required to obtain phase pure samples, depending on the value

12

of  $x$ . The  $0 \leq x \leq 0.1$  compositions were prepared in an inert argon atmosphere at 700 °C and

13

had a monoclinically distorted O'3 type structure. The  $0.25 \leq x \leq 0.33$  compositions were

14

prepared in air at 850 °C and had a P2-type structure. Compositions in the range of  $0.5 \leq x \leq$

15

0.66 were synthesized in air at 850 °C and had an O3-type structure. Lastly, compositions with

16

$0.9 \leq x \leq 1$  were prepared in an oxygen atmosphere at 700 °C and had a monoclinically distorted

17

O'3 type structure. Electrochemical experiments were performed on pure phase samples. All

18

showed reversibility of sodium ions and high capacities. The highest reversible capacity was

19

achieved for  $x = 0.66$ , with a capacity of  $\sim 190$  mAh/g and an average discharge voltage of 3.07

20

V, corresponding to a high energy density of 2705 Wh/L. This is among the highest reported

21

volumetric energy densities for Na-ion battery electrodes.

22

23

**Introduction**

24 Sodium-ion batteries that comprise electrode materials derived from low cost and earth  
25 abundant raw materials have been proposed as an alternative to Lithium-ion batteries.<sup>1,2</sup> Layered  
26 oxides derived from the rock salt structure are often amenable towards reversible intercalation  
27 and have garnered interest in recent years for their application as cathode intercalation materials  
28 for sodium-ion batteries.<sup>3-6</sup> Structures of layered  $\text{AMO}_2$  oxides (A is an alkali metal and M is a  
29 transition metal or a mixture of transition metals) have been categorized according to their  
30 layered stacking sequence and the geometry of the alkali metal ion site by Delmas.<sup>7</sup> This  
31 notation is followed here. Common layered  $\text{AMO}_2$  oxides have a rhombohedral  $\text{O}3$  type,  
32 monoclinic  $\text{O}'3$  type, or hexagonal  $\text{P}2$  type structure. These common structure types are shown  
33 in Figure 1.

34 The  $\text{NaMO}_2$  oxides generally form layered structures quite easily due to the large ionic  
35 size of  $\text{Na}^+$ , which reduces electrostatic repulsion between the oxide layers.<sup>8</sup> This is not always  
36 true in the case of  $\text{LiMO}_2$  oxides, which can be susceptible to cation mixing or conversion to  
37 spinel structures. For example, layered  $\text{LiNi}_{0.5}\text{Mn}_{0.5}\text{O}_2$  has been studied as a cathode material for  
38 lithium-ion batteries, however it suffers from cation mixing.<sup>9-11</sup> This is due to the similarity of  
39 ionic size of  $\text{Li}^+$  and  $\text{Ni}^{2+}$ .<sup>12</sup> However, in  $\text{NaNi}_x\text{Mn}_{1-x}\text{O}_2$  cation mixing between sodium and the  
40 transition metals does not occur, as sodium has a significantly larger ionic radius than the  
41 transition metal ions. Because of the extra stability of layered  $\text{AMO}_2$  oxides with large alkali  
42 metal cations (A), they can often accommodate significantly more deficiency in the alkali metal  
43 layer, when A is not lithium.<sup>8</sup> This allows such materials to have high capacity while still  
44 maintaining their structural integrity.

45 A number of studies have investigated compositions that fall within the  $\text{NaNi}_x\text{Mn}_{1-x}\text{O}_2$   
46 series and their use as cathodes in sodium ion batteries, however no systematic study of this

47 system has been reported. Parant et al. studied the structures of  $\text{Na}_x\text{MnO}_2$  ( $x = 0.2, 0.40, 0.44,$   
48  $0.70, 1$ ) made by solid state methods.<sup>13</sup>  $\text{NaMnO}_2$  was found to form a low temperature  
49 monoclinic  $\alpha\text{-NaMnO}_2$  phase (which is denoted here as O'3  $\text{NaMnO}_2$ ), and a high temperature  
50 orthorhombic phase ( $\beta\text{-NaMnO}_2$ ). Mendiboure et al. investigated the structural transitions  
51 induced by electrochemical desodiation of  $\text{NaMnO}_2$  bronzes in 1M  $\text{NaClO}_4$  in PC electrolyte.<sup>14</sup>  
52 They found that for  $\text{Na}_{0.70}\text{MnO}_2$  the P2 structure is maintained from  $0.45 \leq x \leq 0.85$ , while both  
53 the O'3  $\alpha\text{-NaMnO}_2$  and  $\beta\text{-NaMnO}_2$  show two structural transitions during cycling. Ma et al.  
54 measured the electrochemical performance of O'3  $\text{NaMnO}_2$  in 1M  $\text{NaPF}_6$  in EC:DMC  
55 electrolyte<sup>15</sup> and obtained significantly higher capacities compared to Mendiboure et al. They  
56 claimed that this improved result was due to the difference in electrolyte used. The voltage  
57 curve of O'3  $\text{NaMnO}_2$  was found to comprise many pronounced features with strong voltage  
58 steps and plateaus indicative of phase transitions. The sequence of phase transitions during  
59 charge and discharge were found not to be the same, indicating that the charge and discharge  
60 processes go through different reaction paths. However, this hysteresis was found to be  
61 reversible. After 20 charge/discharge cycles 132 mAh/g capacity was retained from a 185  
62 mAh/g first discharge capacity.<sup>15</sup>

63 The electrochemistry of O'3  $\text{NaNiO}_2$  has been studied by Braconnier et al. in 1M  $\text{NaClO}_4$   
64 in PC electrolyte.<sup>16</sup> Only 0.2 Na could be removed during electrochemical desodiation.  
65 Recently Vassilaras et al. reinvestigated the electrochemistry of O'3  $\text{NaNiO}_2$  in 1M  $\text{NaPF}_6$  in  
66 EC:DMC electrolyte and achieved a reversible discharge capacity of 120 mAh/g (corresponding  
67 to the removal of about 0.5 Na).<sup>17</sup> The voltage curve of O'3  $\text{NaNiO}_2$  was found to comprise a  
68 number of plateaus which are completely reversible.

69 Paulsen and Dahn studied the layered manganese bronzes,  $\text{Na}_{2/3}[\text{Mn}_{1-x}\text{M}_x]\text{O}_2$  with the P2-  
70 structure.<sup>18</sup>  $\text{Na}_{2/3}[\text{Mn}_{1-x}\text{Ni}_x]\text{O}_2$  could be made phase pure at compositions up to  $x = 1/5$ . Higher  
71 nickel contents resulted in phases coexisting with NiO. It was reasoned that this behavior could  
72 be understood if  $\text{Ni}^{2+}$  replaces  $\text{Mn}^{3+}$  to make  $\text{Na}^{+}_{2/3}[\text{Mn}^{3+}_{1-3x}\text{Mn}^{4+}_{2x}\text{Ni}^{2+}_x]\text{O}_2$ , then the composition  
73 limit is reached at  $x = 1/5$ . For compositions with  $x < 1/5$ , the oxidation state of Mn is less than  
74 3.5, which results in an orthorhombic distortion of the P2 structure due to the co-operative Jahn-  
75 Teller effect. At compositions with  $x > 1/5$ , an undistorted P2 structure was obtained.

76 Lu and Dahn studied the electrochemical extraction and insertion of sodium in P2-  
77  $\text{Na}_{2/3}\text{Ni}_{1/3}\text{Mn}_{2/3}\text{O}_2$  by in situ x-ray diffraction.<sup>19</sup> They found that the Na can be completely  
78 extracted from this material and reversibly inserted again. When  $x > 1/3$  the structure is P2. At  $x$   
79  $= 1/3$  a small amount of O2 structure is observed. For  $x < 1/3$  the structure adopts the P2  
80 structure, with some minor O2 and  $\text{Ni}_{1/3}\text{Mn}_{2/3}\text{O}_2$  phases also present. O3  $\text{NaNi}_{1/2}\text{Mn}_{1/2}\text{O}_2$  has  
81 been studied extensively by Komaba et al.<sup>20-22</sup> This material has a first discharge capacity of  
82 185 mAh/g, between 2.2 – 4.5 V and a density of 4.59 g/mL. This corresponds to a volumetric  
83 energy density of 2700 Wh/L vs Na, which is similar to the energy density of  $\text{LiNi}_{1/3}\text{Mn}_{1/3}\text{Co}_{1/3}\text{O}_2$   
84 vs Li. However, the reversibility of O3  $\text{NaNi}_{1/2}\text{Mn}_{1/2}\text{O}_2$  cycled in this voltage range is poor. If  
85 the upper voltage window is narrowed to 3.8 V then 125 mAh/g is achieved with good capacity  
86 retention. During cycling the O3 starting material changes to the O'3, P3, P'3, and then P3"  
87 structures.

88 The high capacities and stable cycling obtained in cathodes containing Ni and Mn make  
89 such electrodes attractive for use in commercial applications. To more fully explore the  
90 properties of these materials a synthetic, structural and electrochemical study of the entire  
91  $\text{NaNi}_x\text{Mn}_{1-x}\text{O}_2$  ( $0 \leq x \leq 1$ ) system is needed, and was undertaken herein. Using a number of

92 synthetic conditions, it was found that phase pure materials could only be obtained for  $x = 0$ ,  
93  $0.25 \leq x \leq 0.66$  and  $x = 1$ . The phases obtained during synthesis depended strongly on the  
94 precursor materials and the oxygen partial pressure during their heating. To our knowledge this  
95 is first report of the single-phase oxides with  $x = 0.25$  and  $x = 0.66$ . The electrochemical  
96 performance of phase pure materials was evaluated in sodium cells. These materials were found  
97 to reversibly intercalate sodium and have a high tolerance towards sodium vacancies, leading to  
98 high gravimetric capacities and energy densities.

99

## 100 **Experimental**

101  $\text{NaNi}_x\text{Mn}_{1-x}\text{O}_2$  materials were prepared via solid-state reactions. Phase pure samples  
102 proved difficult to produce. Upwards of 300 samples were synthesized in order to determine  
103 synthesis conditions that would give phase pure samples, as synthesis was not trivial. It was  
104 found that the synthesis conditions strongly affected the phases obtained, including the precursor  
105 material composition, the mixing and/or grinding method, powder preparation (pelletization),  
106 heating temperature, heating atmosphere, and quenching rate. The precursors used in the  
107 syntheses were:  $\text{Na}_2\text{CO}_3$  (BioXtra,  $\geq 99.0\%$  Sigma Aldrich), NiO ( $-325$  mesh, 99 % Alfa Aesar),  
108  $\text{Mn}_2\text{O}_3$  ( $-325$  mesh, 99 %, Sigma Aldrich),  $\text{MnO}_2$  (*ReagentPlus*<sup>®</sup>, 60 - 230 mesh,  $\geq 99\%$ , Sigma  
109 Aldrich), and  $\text{Na}_2\text{O}_2$  (granular, + 140 mesh particle size, 97 %, Sigma-Aldrich). This method  
110 differs from previous reports, which used mixed transition metal hydroxides as precursors.<sup>19,20</sup>  
111 An excess amount of the sodium containing precursors (usually 10 % weight) was added to  
112 compensate for the loss of sodium due to its volatility at the high reaction temperatures. For this  
113 reason the stated sodium compositions of these samples are nominal.

114 Different precursor combinations and heating conditions were found to be the most  
115 effective for obtaining phase pure samples, depending on the composition range in  $\text{NaNi}_x\text{Mn}_{1-x}\text{O}_2$ . For  $0 \leq x \leq 0.05$ ,  $\text{Na}_2\text{CO}_3$ ,  $\text{NiO}$ , and  $\text{MnO}_2$  were ball milled for a half hour and the powder  
116 was then fired at  $800\text{ }^\circ\text{C}$  in argon for 10 hours. For  $0.25 \leq x \leq 0.66$ ,  $\text{Na}_2\text{CO}_3$ ,  $\text{NiO}$  and  $\text{Mn}_2\text{O}_3$   
117 were ball milled for one hour and pelletized before heating in air at  $850\text{ }^\circ\text{C}$  for 24 hours,  
118 followed by quenching in liquid nitrogen. Samples with compositions in the range of  $0.95 \leq x \leq$   
119  $1$  used  $\text{Na}_2\text{O}_2$ ,  $\text{NiO}$  and  $\text{Mn}_2\text{O}_3$  as precursors that were ball milled for a half hour and then fired  
120 in oxygen at  $700\text{ }^\circ\text{C}$  for 12 hours. Minimal iron contamination is expected to be present in these  
121 samples due to milling in a hardened steel vessel, however this was not assessed. Table 1  
122 summarizes the three synthesis methods that resulted in phase pure products for the various  
123 composition ranges. These synthesis methods will be referred to as Method A, B and C, as  
124 denoted in Table 1. After synthesis the samples were transferred directly in an argon filled  
125 glovebox to avoid air exposure, as the samples were found to be hygroscopic. All subsequent  
126 powder handling (X-ray measurement, electrode and coin cell preparation) was performed under  
127 an inert atmosphere.  
128

129 X-ray powder diffraction (XRD) measurements were made with a Siemens D500 powder  
130 diffractometer equipped with a Cu target X-ray tube and a diffracted beam monochromator.  
131 Powder samples were measured in a gas tight X-ray sample holder (DPM Solutions, Hebbville  
132 NS), shown in Figure 2. The sample holder had an aluminized Mylar window mounted in an arc  
133 such that it was perpendicular to the incident and scattered x-ray beam and did not contribute to  
134 the measured XRD patterns. A continuous flow of helium gas was provided through the sample  
135 holder diffraction measurements to maintain an inert atmosphere and increase counts. Rietveld  
136 refinement and profile matching of the powder diffraction data were performed using the

137 computer program Rietica. A Phenom G2-pro scanning electron microscope (SEM,  
138 Nanoscience, Arizona) was used to determine particle size and morphology of the powder  
139 samples.

140 Electrodes for electrochemical measurements consisted of  $\text{NaNi}_x\text{Mn}_{1-x}\text{O}_2$  powder, carbon  
141 black (Super P, Erachem Europe), and PVdF (polyvinylidene fluoride, Kynar HSV 900) in an  
142 8:1:1 weight ratio. These components were thoroughly mixed in N-methyl-2-pyrrolidone (Sigma  
143 Aldrich, anhydrous 99.5%) with two tungsten carbide balls in a Retsch PM200 rotary mill (200  
144 rpm, 1 hour) to create uniform black slurries. The slurries were then coated onto aluminum foil  
145 and dried under vacuum at 120 °C for 2 hours. 2 cm<sup>2</sup> circular electrodes were punched from the  
146 resulting coatings and incorporated into 2325 type coin cells. Circular Na foil counter/reference  
147 electrode disks were punched from thin foil (0.015 inch) that was rolled from sodium ingot  
148 (Sigma Aldrich, ACS reagent grade). 1 M  $\text{NaPF}_6$  (Sigma Aldrich 98%) dissolved in propylene  
149 carbonate (Novolyte Technologies) was used as electrolyte. Two Celgard 3501 and one BMF  
150 (blown microfiber separator, 3M Company) were used as separators. Cells were tested with a  
151 Maccor Series 4000 Automated cycler and were typically cycled between 2.0 V and 4.3 V at a  
152 constant current of C/10, calculated based on the theoretical capacity corresponding to the  
153 desodiation of all of the sodium from the positive electrode.

154 Samples were dissolved in aqua regia acid in order to perform Inductively coupled  
155 plasma (ICP) analysis using a Varian Vista Pro (radial view) ICP OES instrument located in the  
156 Materials Engineering Centre at Dalhousie University. This analysis allowed the accurate  
157 determination of atomic ratios within the powder samples.

## 158 **Results and Discussion**

## 159 **Phase Behavior in the $\text{NaNi}_x\text{Mn}_{1-x}\text{O}_2$ System**

160 Figure 3 shows an SEM image of  $\text{NaNi}_x\text{Mn}_{1-x}\text{O}_2$  with  $x = 2/3$ , which is typical of the  
161 samples made here. The particles have a thin hexagonal plate like morphology and are about 1 -  
162  $2 \mu\text{m}$  in size. Figures 4 - 6 show the XRD patterns of samples prepared by methods A, B and C,  
163 respectively. All diffraction patterns of layered phases could be refined using either a  
164 monoclinic (O'3 type, C2/m), rhombohedral (O3 type, R3m) or hexagonal (P2 type, P6<sub>3</sub>/mmc)  
165 space group. In some cases a NiO impurity was detected as peaks near  $43^\circ$ . XRD patterns  
166 indicative of phase pure samples are highlighted in Figures 4 - 6. Figure 7 summarizes the  
167 phases observed for samples prepared by methods A, B and C as a function of  $x$  in  $\text{NaNi}_x\text{Mn}_{1-x}$   
168  $\text{O}_2$ . The phase boundaries were drawn to roughly correspond to the phase behavior considering  
169 the limited of number of sample compositions analyzed.

170 Method A was the only method used that resulted in phase pure O'3  $\text{NaMnO}_2$ , as shown  
171 in Figure 4. However, this method did not result in phase pure samples for  $x > 0$ . Instead,  
172 increasing the nickel content in the range of  $0.05 \leq x \leq 0.25$ , led to a monoclinic structure mixed  
173 with a distorted P2 structure.

174 Method B resulted in phase pure samples having the P2 structure for  $0.25 \leq x \leq 0.33$ , as  
175 shown in Figure 5. In addition, phase pure samples having the O3 structure were obtained for  $x$   
176  $= 0.5$  and  $0.66$ . Samples with higher nickel content contained increasing amounts of NiO in  
177 addition to the O3 phase. When  $x = 1$  only a NiO phase was present. This is likely a  
178 consequence of significant sodium evaporation, in the form of sodium oxide, from the sample /  
179 precursors during the heating step in air. This is directly related to the synthesis temperature and  
180 length of heating time. Higher synthesis temperatures are needed for product formation, however  
181 when temperatures of  $900^\circ\text{C}$  or above are used significant sodium evaporation occurs and a NiO



182 phase is observed. If longer heating times ( $> 24$  hours) are used sodium evaporation is also  
183 increased and in many cases no ordered layered phases are formed.

184 When samples were prepared using method C, phase pure samples having the P2  
185 structure were obtained for  $0.25 \leq x \leq 0.33$ , as shown in Figure 6. Phase pure O'3  $\text{NaNiO}_2$  of the  
186 O'3 type was also obtained when  $x = 1$ . Method C was the only method used that resulted in  
187 phase pure O'3  $\text{NaNiO}_2$ . Outside these composition ranges, method C did not result in phase  
188 pure samples. Samples with  $0.33 < x < 0.66$  consisted of a mixture of O3  $\text{NaNi}_x\text{Mn}_{1-x}\text{O}_2$  and  
189 NiO, while samples with  $0.66 < x < 1$  consisted of O'3  $\text{NaNi}_x\text{Mn}_{1-x}\text{O}_2$  and NiO. The phase  
190 boundary at  $x = 0.66$  is bothersome as NiO is observed on either side of the boundary. This  
191 appears to violate the Gibbs phase rule for a binary system, but sodium evaporation adds another  
192 degree of freedom to the system.

193 By selecting one of the methods, A, B, or C, phase pure  $\text{NaNi}_x\text{Mn}_{1-x}\text{O}_2$  could be made for  
194  $x = 0$ ,  $0.25 \leq x \leq 0.66$ , and  $x = 1$ . A 2-phase region exists between O'3  $\text{NaMnO}_2$  and P2  
195  $\text{NaNi}_{0.25}\text{Mn}_{0.75}\text{O}_2$ , while the  $0.66 < x < 1$  composition range seems to lie in a 3-phase  
196  $\text{NaNi}_{0.66}\text{Mn}_{0.33}\text{O}_2$  - NiO -  $\text{NaNiO}_2$  coexistence region in our synthesis conditions. We believe  
197 the co-operative Jahn Teller distortion in the O'3  $\text{NaMnO}_2$  and O'3  $\text{NaNiO}_2$  end members of this  
198 composition series induces phase separations with non-distorted phases, rather than forming  
199 intermediate phases with internal stresses.

200 Figure 8 shows the structural relationship between the O'3 and O3 unit cells. The  
201 monoclinic distortion of the O3 occurs due to the presence of Jahn-Teller ions. Rietveld  
202 refinements were performed on all samples to obtain lattice constants. Examples of these  
203 refinements are shown in Figures 9 and 10 for the compositions with  $x = 0.66$  and  $0.25$ ,  
204 respectively. The crystallographic data for these compositions are summarized in Tables 2 and

205 3, respectively. For  $x = 0.66$  the O3  $\alpha$ -NaFeO<sub>2</sub> (space group  $R\bar{3}m$ ) structure type was used to  
206 refine the XRD pattern. In initial refinements Na and Ni were allowed to mix, however the  
207 degree of cation mixing was found to be only 0.7 %. This indicates that there was relatively little  
208 cation mixing, which is typical of NaMO<sub>2</sub> materials. This can be attributed to the difference in  
209 ionic radius of Na<sup>+</sup> (1.02 Å) and Ni<sup>2+</sup> (0.69 Å), which would tend to make cation mixing  
210 unfavorable.<sup>12</sup> Therefore cation mixing was not considered in the final refinements. For  $x =$   
211 0.25, the P2  $\beta$ -RbScO<sub>2</sub> structure type (space group  $P6_3/mmc$ ) was used to refine the XRD  
212 measurements. The lattice parameters and site occupancies agree with what has been reported  
213 by Delmas and Werner.<sup>23</sup> A relatively high R-factor was obtained for this P2 structure which is  
214 attributed to the presence of unrefined peaks at low angles, which likely arise from superlattice  
215 ordering.

216 Due to the high volatility of Na at the high reaction temperatures employed here the  
217 atomic ratios of the products found from XRD refinement were verified via ICP analysis. The  
218 ICP results show good agreement with the anticipated atomic ratios for all pure phase samples,  
219 with the Na and TM atomic ratios only varying from the anticipated ratios at most  $\pm 3$  %.

220 When the monoclinic structures with  $x = 0$  and 1 were refined, two separate M-O bond  
221 lengths in the MO<sub>6</sub> octahedra were observed, which is characteristic of the Mn<sup>3+</sup> (d<sup>4</sup> high-spin)  
222 and Ni<sup>3+</sup> (d<sup>7</sup> low-spin) Jahn-Teller ions. NaMnO<sub>2</sub> has Mn-O bond lengths of 1.93 Å (x4) and  
223 2.40 Å (x2). NaNiO<sub>2</sub> has Ni-O bond lengths of 2.02 Å (x4) and 2.22 Å (x2). These distortions  
224 will result in variation from the ideal hexagonal  $a/b$  ratio of  $\sqrt{3}$  (1.732) and  $\beta$  angle of 109.11°,  
225 leading to a monoclinic distortion of the layered structure. This is seen clearly from the lattice  
226 parameters of the NaMnO<sub>2</sub>;  $a = 5.67$  Å,  $b = 2.86$  Å and  $\beta$  angle = 113.2, where  $a/b = 1.98$ .  
227 These are similar to results reported by the Ceder group.<sup>15,17</sup> Table 4 summarizes the cell

228 parameters that were used to fit all of the as prepared single phase samples. Values from past  
 229 studies are also included and they are in close approximation to those found in this work.

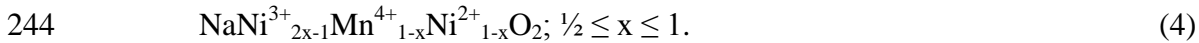
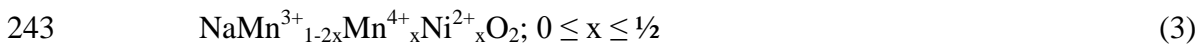
230 Figure 11 shows the lattice parameters of the phase pure  $\text{NaNi}_x\text{Mn}_{1-x}\text{O}_2$  compositions  
 231 obtained as a function of  $x$ . In order to make comparisons all structures were indexed according  
 232 to the hexagonal O3 lattice using the following relations:

$$233 \quad O'3 \rightarrow O3: \quad a_1 = \sqrt{\left(\frac{a_m}{2}\right)^2 + \left(\frac{b_m}{2}\right)^2}; \quad a_2 = b_m; \quad c = 3c_m \sin \beta \quad (1)$$

$$234 \quad P2 \rightarrow O3: \quad a = b = a_{P2}; \quad c = \frac{3}{2}c_{P2} \quad (2)$$

235 where  $a$ ,  $b$ , and  $c$  are lattice constants with respect to the O3 unit cell,  $a_m$ ,  $b_m$ ,  $c_m$  and  $\beta$  are the O'3  
 236 unit cell parameters and  $a_{P2}$ ,  $b_{P2}$ ,  $c_{P2}$  are the P2 unit cell parameters. Using this formalism, the  
 237 O'3 lattice will have two non-equivalent  $a$  lattice constants, denoted as  $a_1$  and  $a_2$ . Lattice  
 238 constants from previous studies are also plotted on Figure 11, and are in good agreement with  
 239 results herein. Generally, as  $x$  increases  $a$  increases and  $c$  decreases. Some discontinuities in  
 240 these parameters are present at the structural phase boundaries.

241 To understand the trends in the lattice constants and structural changes it is first  
 242 convenient to assume the transition metal oxidation states are as follows:



245 This formalism can explain the different phases observed, as shown in Figure 7. When  $x = 0$ , all  
 246 the manganese is present as  $\text{Mn}^{3+}$ , resulting in a co-operative Jahn-Teller distortion and  $\text{NaMnO}_2$   
 247 having a monoclinic phase. Typically such a distortion persists while the average oxidation state  
 248 remains below 3.5, as it does in  $\text{Na}_{2/3}[\text{Mn}_{1-y}\text{Ni}_y]\text{O}_2$  for  $0 < y < 1/6$ , in which a distorted P'2  
 249 structure is formed.<sup>18</sup> Such a distorted P'2 phase was not observed here. Although the average

250 oxidation state of Mn is below 3.5 for  $x < \frac{1}{3}$ , the system prefers to form a 2-phase region  
251 between monoclinic  $\text{NaMnO}_2$  and an ideal P2 structure for  $0 < x < \frac{1}{4}$ . For  $\frac{1}{3} < x < \frac{2}{3}$  the lattice  
252 remains fully symmetric as the O3 phase. For  $\frac{2}{3} < x < 1$  the system again prefers adopting a 2-  
253 phase state as a response to increasing amounts of the  $\text{Ni}^{3+}$  Jahn-Teller ion, instead of adopting a  
254 distorted structure.

255 The change in the  $a$  lattice constant is typically attributed to the difference in radii of the  
256 different ions in the transition metal layer. In this case where  $a$  increases with increasing Ni  
257 content this argument cannot be made because as  $x$  increases each  $\text{Mn}^{3+}$  (0.645 Å) is replaced by  
258 a  $\text{Ni}^{2+}$  (0.69 Å) and a  $\text{Mn}^{4+}$  (0.53 Å), which have a lower average ionic radius.<sup>12</sup> The variation in  
259 the  $c$  lattice constant with  $x$  is likely due to the packing efficiency between the different  
260 structures. The O'3 and O3 all have similar  $c$  values while the less efficient packing of the P2  
261 structures cause them to have much higher  $c$  lattice constants. Overall the changes in lattice the  
262 constants result in the little changes in the density for the P2 and O3 compositions ( $0.2 \leq x \leq$   
263  $0.67$ ), which is about 4.63 g/mL in this range of  $x$ . The density of  $\text{NaMnO}_2$  is much less than  
264 this, presumably due to the large monoclinic distortion in the structure.

## 265 **Electrochemical Characteristics**

266 Figure 12 shows the voltage curves of the phase pure  $\text{NaNi}_x\text{Mn}_{1-x}\text{O}_2$  materials that were  
267 prepared. There are several plateaus which appear for each composition and they are similar for  
268 both charge and discharge (except for the first charge in some compositions), indicating  
269 reversible processes. The step like character of the many plateaus is expected for these sodium  
270 containing materials.<sup>24</sup> In general sodium intercalation materials tend to have more phase  
271 transitions than the lithium containing ones. This is likely due to the strain effects of the larger  
272  $\text{Na}^+$  ions which produce ordering interactions.

273 Many of the compositions in the  $\text{NaNi}_x\text{Mn}_{1-x}\text{O}_2$  series display a high first discharge  
274 capacity. The highest first discharge capacity was for  $x = 0.66$ , with a capacity of  $\sim 190$  mAh/g.  
275 It should be noted that all of these materials have high first cycle irreversible capacities, except  
276 for  $x = 0.33$  and  $0.5$ . Electrolyte decomposition above  $4$  V could contribute to these high  
277 irreversible capacities, which can be somewhat suppressed when the upper voltage limit is  
278 lowered. NMR studies could be performed after cycling to determine whether electrolyte  
279 decomposition has occurred. It is anticipated that other factors could contribute to these high  
280 irreversible capacities, such as irreversible material changes during cycling.

281 Figure 13 shows the specific discharge capacities with cycle number for  $\text{NaNi}_x\text{Mn}_{1-x}\text{O}_2$   
282 cycled between  $2.0$  to  $4.3$  V. All compositions, except  $x = 1$ , had capacities greater than  $100$   
283 mAh/g over for  $20$  cycles, but had severe capacity fade. The reversibility of these materials  
284 could be improved by optimization of the electrolyte formulation, as additives such as FEC have  
285 shown to improve cycling.<sup>22</sup> For compositions where there exist results in the literature these  
286 findings show good agreement.<sup>15,17,20</sup> When cycled in this voltage range, the volumetric energy  
287 densities of  $\text{NaNi}_x\text{Mn}_{1-x}\text{O}_2$  ranged from  $1650 - 2705$  Wh/L. The highest volumetric energy  
288 density of  $2705$  Wh/L was achieved for  $x = 0.66$ , with  $190$  mAh/g capacity and an average  
289 discharge voltage of  $3.07$  V. This approaches the energy density of Li-ion cathodes (e.g.  $\sim 2900$   
290 Wh/L for  $\text{LiNi}_{1/3}\text{Mn}_{1/3}\text{Co}_{1/3}\text{O}_2$ ) and is among the highest reported volumetric energy densities for  
291 Na-ion battery electrodes. For example, one of the best known and highest energy density Na-  
292 ion cathode materials, P2- $\text{Na}_{2/3}\text{Fe}_{1/2}\text{Mn}_{1/2}\text{O}_2$ , has a volumetric energy density of  $2132$  Wh/L.<sup>4</sup>

293

294

295 **Conclusions**

296 Phase pure layered  $\text{NaNi}_x\text{Mn}_{1-x}\text{O}_2$  (where  $x = 0, 0.25, 0.33, 0.5, 0.66,$  and  $1$ ) were  
297 synthesized via solid state reactions. Different synthesis conditions were required, depending on  
298 the composition. These materials have a monoclinically distorted  $\text{O}3$  structure ( $x = 0, 1$ ),  $\text{P}2$   
299 structure ( $0.25 \leq x \leq 0.33$ ) or an  $\text{O}3$  structure ( $0.5 \leq x \leq 0.66$ ). Excepting for  $x = 0$ , all  
300 compositions have high densities, above  $4.6 \text{ g/mL}$ . All compositions have high reversible  
301 capacities when cycled between  $2.0$  to  $4.3 \text{ V}$ . The  $x = 0.66$  composition had the highest first  
302 discharge capacity of  $\sim 190 \text{ mAh/g}$  and highest volumetric energy density of  $2705 \text{ Wh/L}$ . This  
303 is one of the highest energy densities reported for Na-ion cathode materials. However, all  
304 compositions had poor cycling performance. Further improvements are required for materials in  
305 this series to be utilized in practical cells.

306

### 307 **Acknowledgements**

308 The authors would like to recognize financial support from 3M Canada and NSERC  
309 under the auspices of the Industrial Research Grants and Discovery Grants programs.

310 **References**

- 311 1. S.-W. Kim, D.-H. Seo, X. Ma, G. Ceder, K. Kang, *Advanced Energy Materials*, **2** (7) , 710  
312 (2012).
- 313 2. A.Y. Tsivadze, T.L. Kulova, A.M. Skundin, *Protection of Metals and Physical Chemistry  
314 of Surfaces*, **49** (2) , 145 (2013).
- 315 3. S. Komaba, C. Takei, T. Nakayama, A. Ogata, N. Yabuuchi, *Electrochemistry  
316 Communications*, **12** (3) , 355 (2010).
- 317 4. N. Yabuuchi, M. Kajiyama, J. Iwatate, H. Nishikawa, S. Hitomi, R. Okuyama, R. Usui, Y.  
318 Yamada, S. Komaba, *Nature Materials*, **11** (6) , 512 (2012).
- 319 5. R. Berthelot, D. Carlier, C. Delmas, *Nature Materials*, **10** (1) , 74 (2011).
- 320 6. Y. Takeda, K. Nakahara, M. Nishijima, N. Imanishi, O. Yamamoto, *Materials Research  
321 Bulletin*, **29** (6) , 659 (1994).
- 322 7. C. Delmas, C. Fouassier, P. Hagenmuller, *Physica*, **99B** , 81 (1980).
- 323 8. C. Delmas, J.J. Braconnier, A. Maazaz, P. Hagenmuller, *Revue de Chimie Minerale*, **1**  
324 (19) , 343 (1982).
- 325 9. J. Reed, G. Ceder, *Electrochemical and Solid-State Letters*, **5** (7) , A145 (2002).
- 326 10. T. Ohzuku, Y. Makimura, *Chemistry Letters*, **2** , 744 (2001).
- 327 11. E. Rossen, C.D.W. Jones, J.R. Dahn, *Solid State Ionics*, **57** , 311 (1992).
- 328 12. R.D. Shannon, *Acta Cryst.*, **A32** , 752 (1976).
- 329 13. J.-P. Parant, R. Olazcuaga, M. Devalette, C. Fouassier, P. Hagenmuller, *Journal of Solid  
330 State Chemistry*, **3** (1) , 1 (1971).
- 331 14. A. Mendiboure, C. Delmas, P. Hagenmuller, *Journal of Solid State Chemistry*, **57** , 323  
332 (1985).
- 333 15. X. Ma, H. Chen, G. Ceder, *Journal of The Electrochemical Society*, **158** (12) , A1307  
334 (2011).
- 335 16. J.-J. Braconnier, C. Delmas, P. Hagenmuller, *Materials Research Bulletin*, **17** (8) , 993  
336 (1982).
- 337 17. P. Vassilaras, X. Ma, X. Li, G. Ceder, *Journal of the Electrochemical Society*, **160** (2) ,  
338 A207 (2012).

- 339 18. J.M. Paulsen, J.R. Dahn, *Solid State Ionics*, **126** , 3 (1999).
- 340 19. Z. Lu, J.R. Dahn, *Journal of The Electrochemical Society*, **148** (11) , A1225 (2001).
- 341 20. S. Komaba, T. Nakayama, A. Ogata, T. Shimizu, C. Takei, S. Takada, A. Hokura, I.  
342 Nakai, *ECS Transactions*, **16** (42) , 43 (2009).
- 343 21. S. Komaba, N. Yabuuchi, T. Nakayama, A. Ogata, T. Ishikawa, I. Nakai, *Inorganic*  
344 *Chemistry*, **51** (11) , 6211 (2012).
- 345 22. S. Komaba, T. Ishikawa, N. Yabuuchi, W. Murata, A. Ito, Y. Ohsawa, *ACS Applied*  
346 *Materials and Interfaces*, **3** , 4165 (2011).
- 347 23. C. Delmas, P. Werner, *Acta Chemica Scandinavica*, **A32** , 329 (1978).
- 348 24. J. Molenda, *Solid State Ionics*, **21** (4) , 263 (1986).
- 349



350 **Table 1**

351

Method	<i>precursors</i>	<i>atmosphere</i>	<i>Annealing temperature</i> (°C)	<i>Annealing time</i> (hours)
A	Na <sub>2</sub> CO <sub>3</sub> , NiO, MnO <sub>2</sub>	Argon	800	10
B	Na <sub>2</sub> CO <sub>3</sub> , NiO, Mn <sub>2</sub> O <sub>3</sub>	Air	850	24
C	Na <sub>2</sub> O <sub>2</sub> , NiO, Mn <sub>2</sub> O <sub>3</sub>	Oxygen	700	12

352

353 Table 1 Synthesis conditions that were utilized to produce pure phase NaNi<sub>x</sub>Mn<sub>1-x</sub>O<sub>2</sub> samples.

354

355 **Table 2**
 $\text{NaNi}_{0.66}\text{Mn}_{0.33}\text{O}_2$  ( $R\bar{3}m$ )

atom	site			x	y	z	occupancy
Na	3b			0	0	0.5	0.988(7)
Ni	3a			0	0	0	0.66
Mn	3a			0	0	0	0.34
O	6c			0	0	0.268(4)	1.0
Cell parameters	a	b	c				
	2.964(5)	2.964(5)	15.810(7)	R-factor		1.99	
	$\alpha$	$\beta$	$\gamma$	R <sub>p</sub>		10.4	
	90	90	120	R <sub>wp</sub>		16.2	

356

357 Table 2 Rietveld refinement results for the  $\text{NaNi}_{0.66}\text{Mn}_{0.33}\text{O}_2$  phase.

358

359 **Table 3**NaNi<sub>0.25</sub>Mn<sub>0.75</sub>O<sub>2</sub> (P6<sub>3</sub>/mmc)

atom	site			x	y	z	occupancy
Na <sub>f</sub>	2b			0	0	0.25	0.331(5)
Na <sub>e</sub>	2d			0.33	0.67	0.75	0.66
Ni	2a			0	0	0	0.25
Mn	2a			0	0	0	0.75
O	4f			0.33	0.67	0.098(2)	1.0
Cell parameters	a	b	c				
	2.887(8)	2.887(8)	11.142(8)	R-factor 4.60			
	α	β	γ	R <sub>p</sub> 19.38			
	90	90	120	R <sub>wp</sub> 29.52			

360

361 Table 3 Rietveld refinement results for the NaNi<sub>0.25</sub>Mn<sub>0.75</sub>O<sub>2</sub> phase.

362

363 **Table 4**

<b>x</b>	<b>Space group</b>	<b>a</b>	<b>b</b>	<b>c</b>	<b><math>\beta</math></b>	<b>M-O bond distance</b>
<b>0</b>	C2/m	5.67, 5.672 [1]	2.86, 2.856 [1]	5.80, 5.807 [1]	113.2, 113.2 [1]	1.93, 2.40 1.94[1], 2.39[1]
<b>0.25</b>	P6 <sub>3</sub> /mmc	2.89	-	11.15	-	1.96
<b>0.33</b>	P6 <sub>3</sub> /mmc	2.89	-	11.07	-	2.002
<b>0.5</b>	R $\bar{3}$ m	2.94, 2.968 [2]	-	15.99, 15.909 [2]	-	2.159
<b>0.66</b>	R $\bar{3}$ m	2.96	-	15.81	-	2.00
<b>1</b>	C2/m	5.34, 5.322 [3]	2.85, 2.845 [3]	5.62, 5.584 [3]	110.5, 110.467 [3]	2.02, 2.22 1.932 [3], 2.177 [3]

364

365 Table 4 Rietveld refinement results for NaNi<sub>x</sub>Mn<sub>1-x</sub>O<sub>2</sub> samples, with literature results, where

366 available, for comparison.

367

368 **Figure Captions**

369

370 Figure 1 P2 (a), O3 (b), and O'3 (monoclinic) (c) structures of  $ABO_2$  layered type oxides. The  
371 unit cell in each diagram is indicated by solid lines. The figures are drawn from the 110  
372 perspective.

373

374 Figure 2 Sample holder used for XRD measurements of air sensitive samples. Holder base (a)  
375 and holder top (b).

376

377 Figure 3 SEM image of  $NaNi_{2/3}Mn_{1/3}O_2$ , showing particle size and morphology.

378

379 Figure 4 X-ray diffraction patterns for samples prepared by method A. The red box highlights  
380 phase-pure samples.

381

382 Figure 5 X-ray diffraction patterns for samples prepared by method B. The red box highlights  
383 phase-pure samples.

384

385 Figure 6 X-ray diffraction patterns for samples prepared by method C. The red box highlights  
386 phase-pure samples.

387

388 Figure 7 A pseudo-binary phase diagram of the  $NaNi_xMn_{1-x}O_2$  system, for samples prepared by  
389 the three synthesis methods as indicated in Table 1.

390

391 Figure 8 An O3 unit cell illustrating the structural relationship between the lattice constants of  
392 the O3 and O'3 phases.

393

394 Figure 9 XRD pattern and Rietveld refinement of phase pure  $\text{NaNi}_{0.66}\text{Mn}_{0.33}\text{O}_2$ . The refined  
395 parameters are summarized in Table 2.

396

397 Figure 10 XRD pattern and Rietveld refinement of the phase pure  $\text{NaNi}_{0.25}\text{Mn}_{0.75}\text{O}_2$ . The refined  
398 parameters are summarized in Table 3.

399

400 Figure 11 Evolution of the lattice parameters  $a$  and  $c$ , as well as the density of  $\text{NaNi}_x\text{Mn}_{1-x}\text{O}_2$  as  
401 a function of  $x$ . All lattice parameters are expressed in terms of the O3 structure, as described in  
402 the text.

403

404 Figure 12 Voltage curves of  $\text{NaNi}_x\text{Mn}_{1-x}\text{O}_2$  at C/10 cycling rate and 30°C. The voltage curves of  
405 the 10<sup>th</sup> cycle are shown as dotted lines.

406

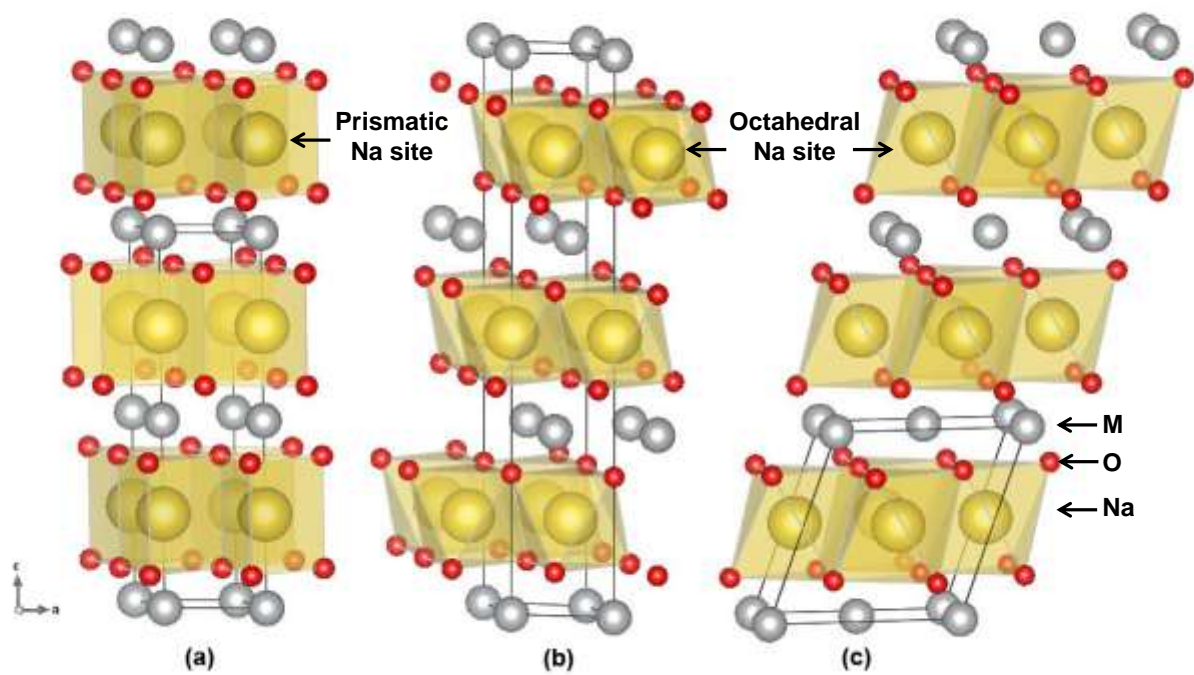
407 Figure 13 The discharge capacities versus cycle number for  $\text{NaNi}_x\text{Mn}_{1-x}\text{O}_2$ . Cells were cycled at  
408 C/10 at 30°C between 2 and 4.3 V.

409

410

411 **Figure 1**

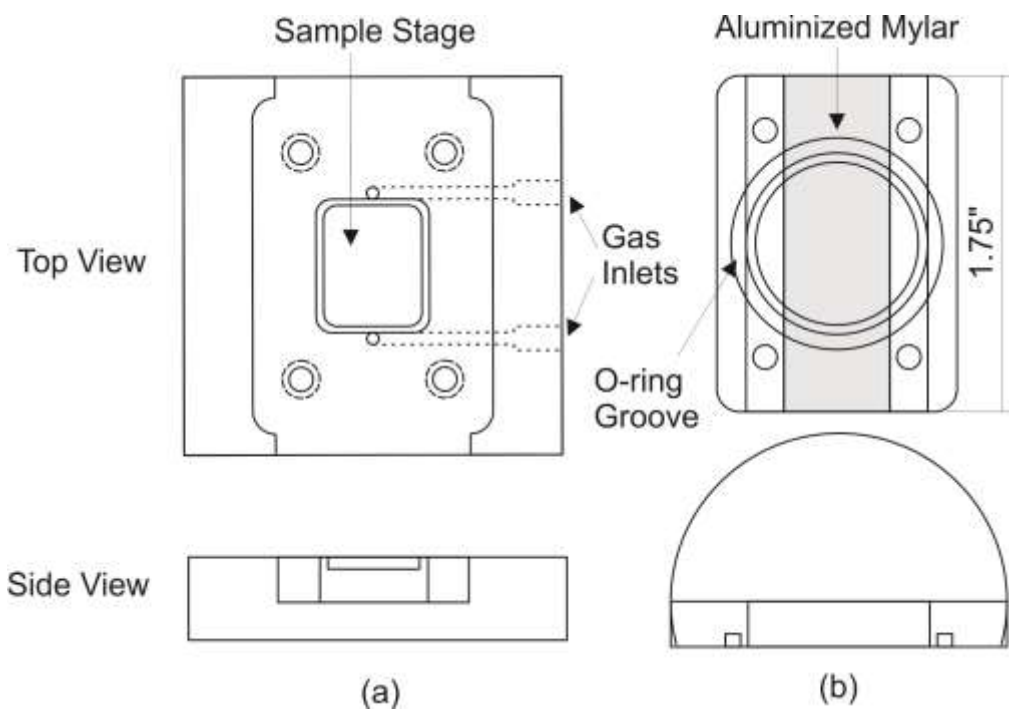
412



413

414 **Figure 2**

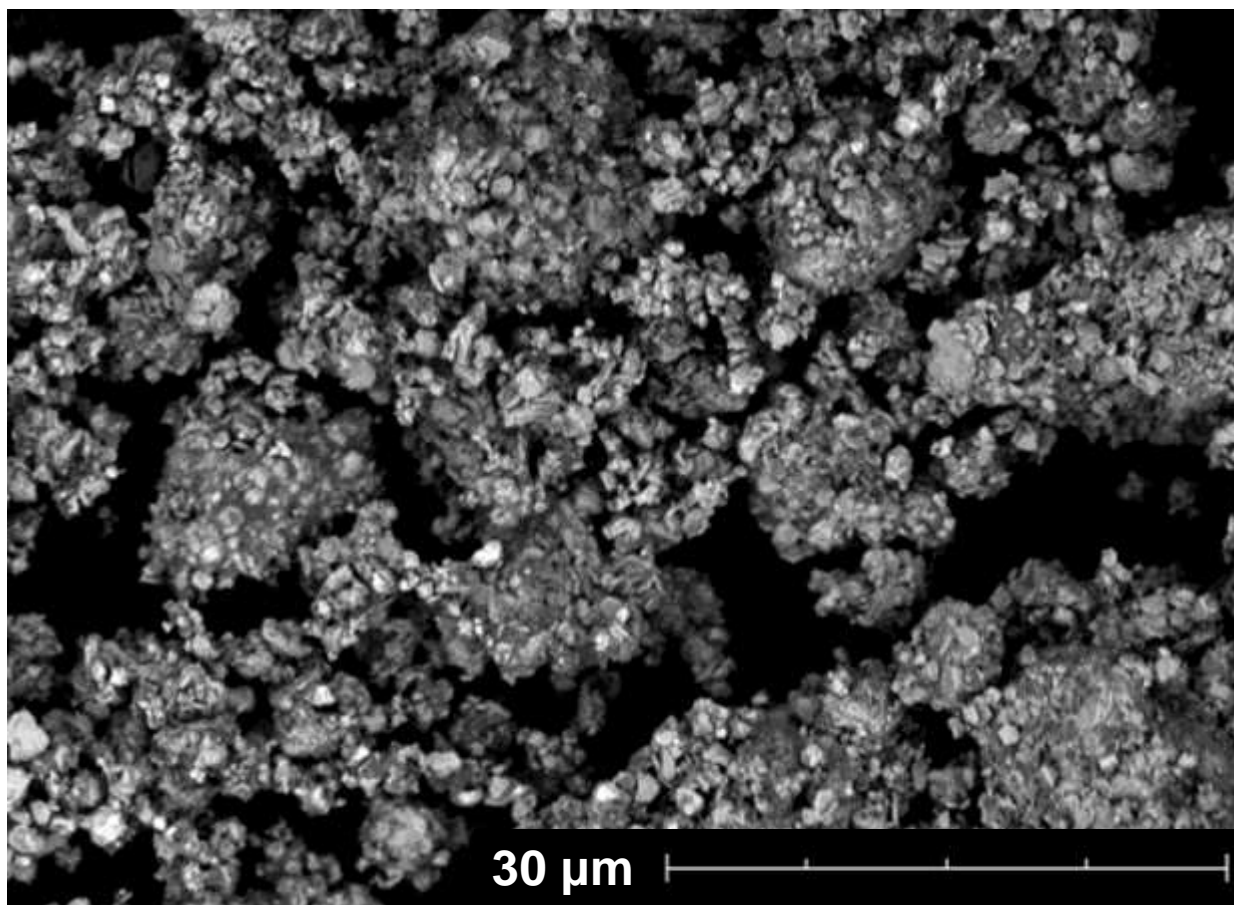
415



416



417 **Figure 3**

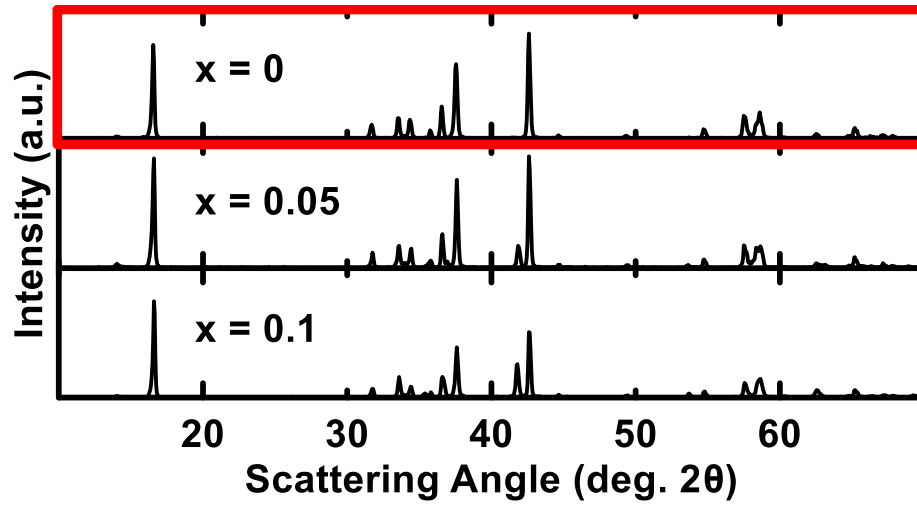


418

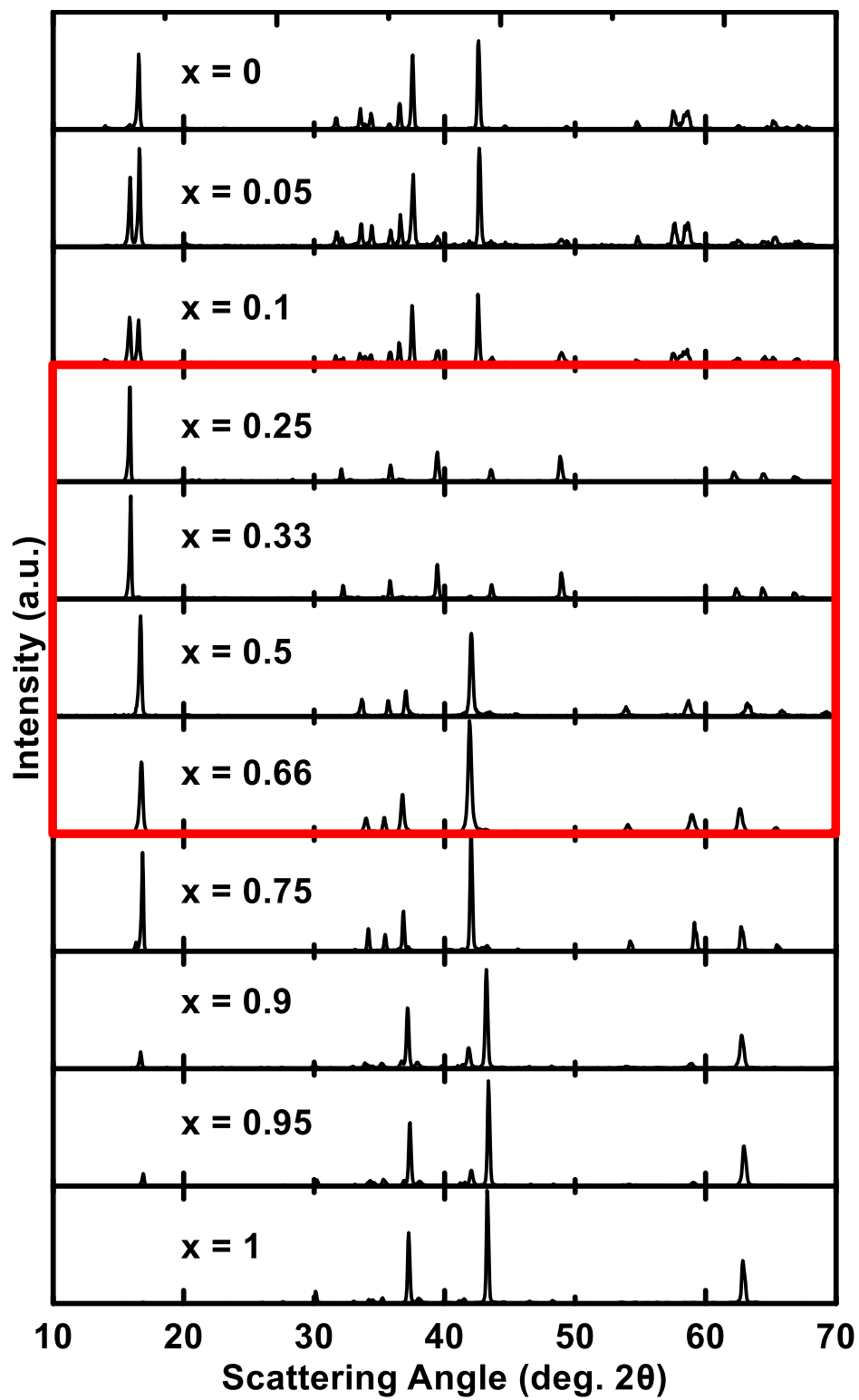
419

420 **Figure 4**

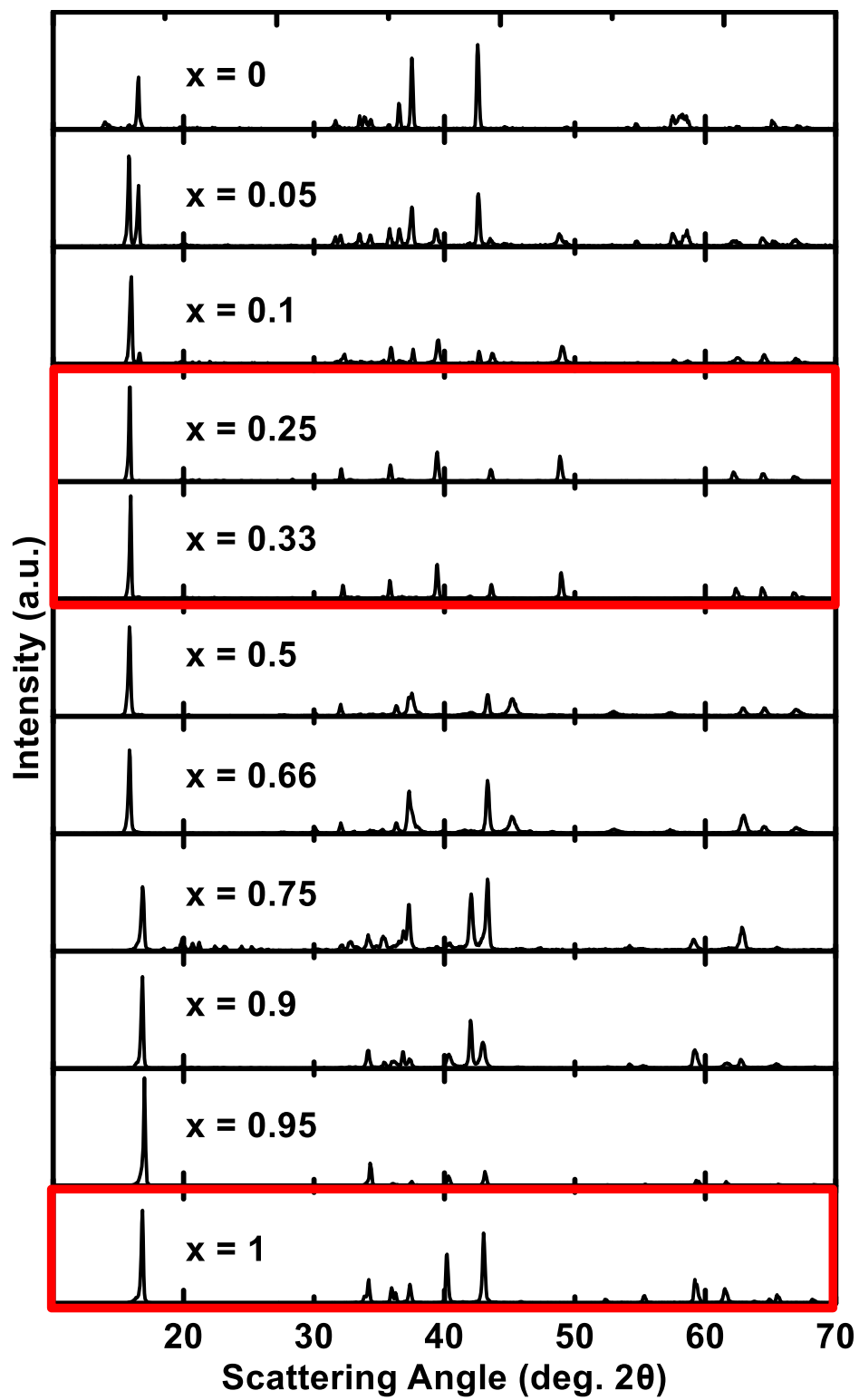
421



422

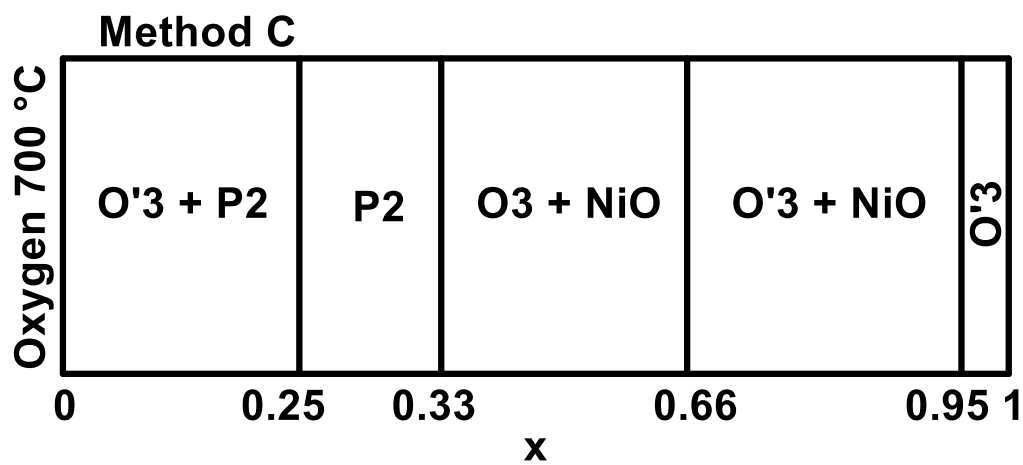
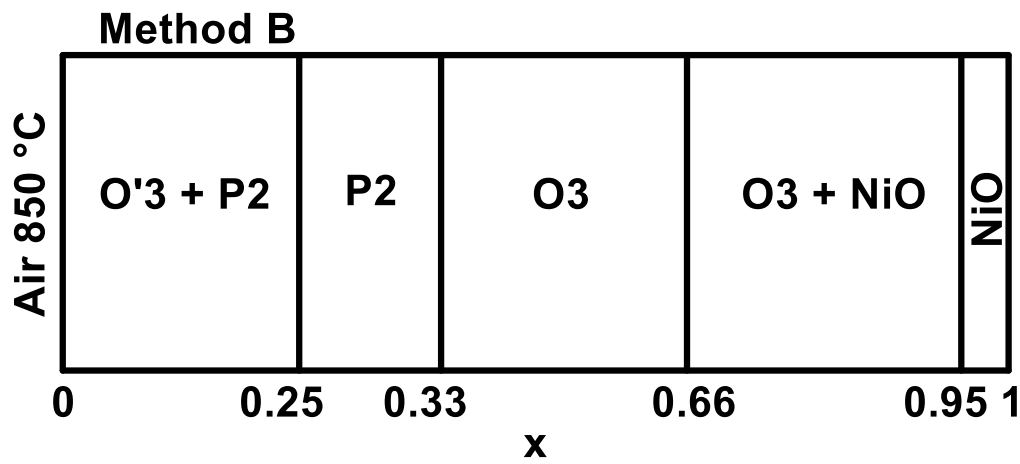
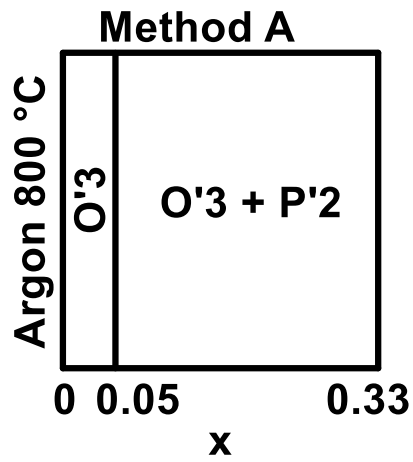


425 **Figure 6**

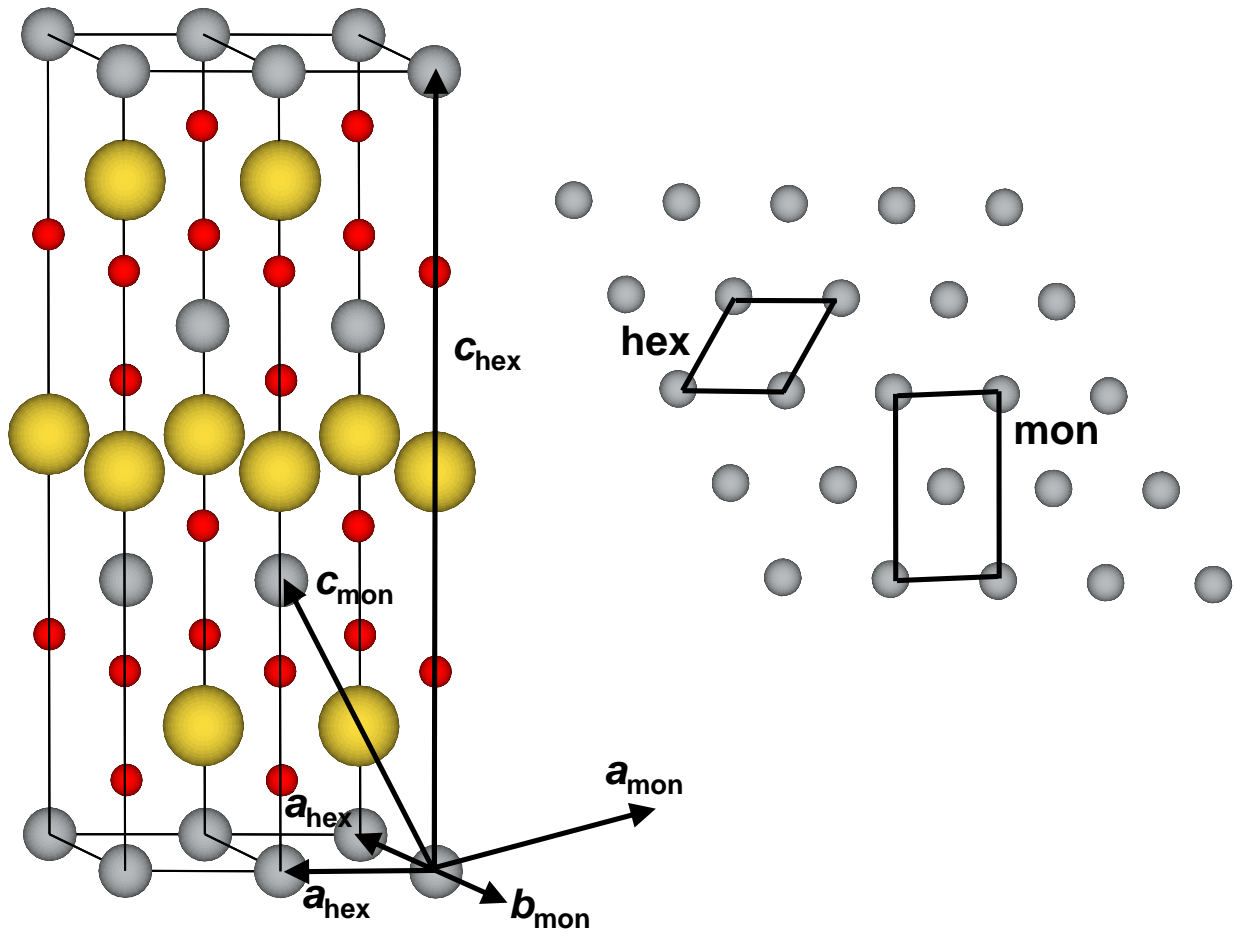


426

427

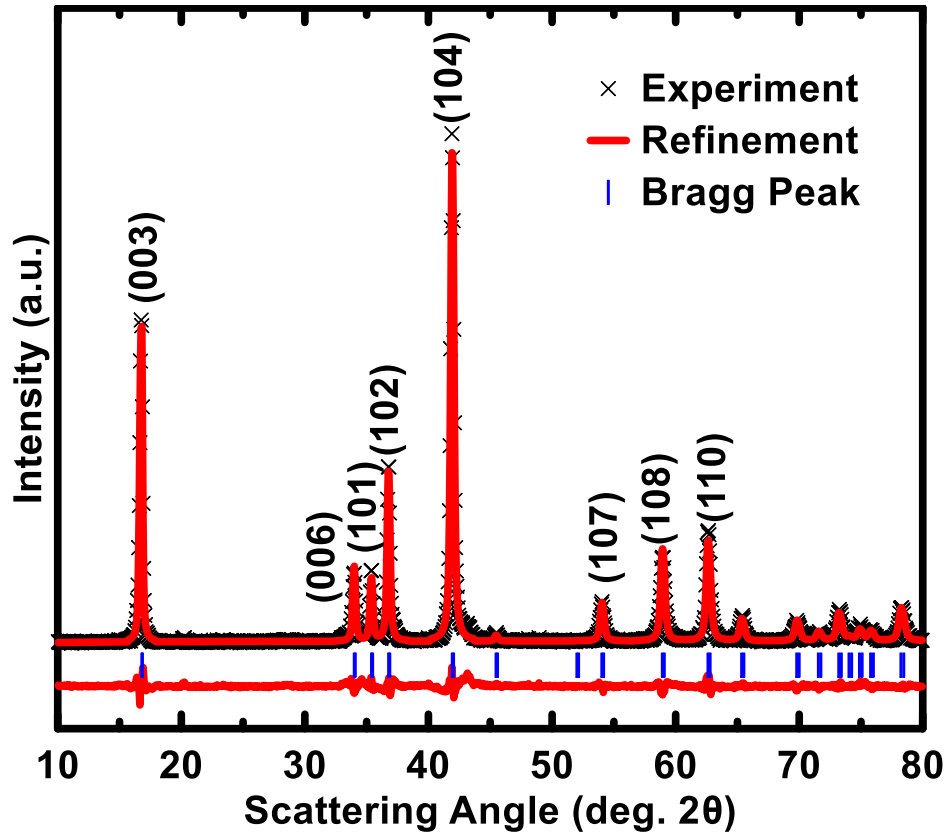


431 **Figure 8**



432  
433

434 Figure 9

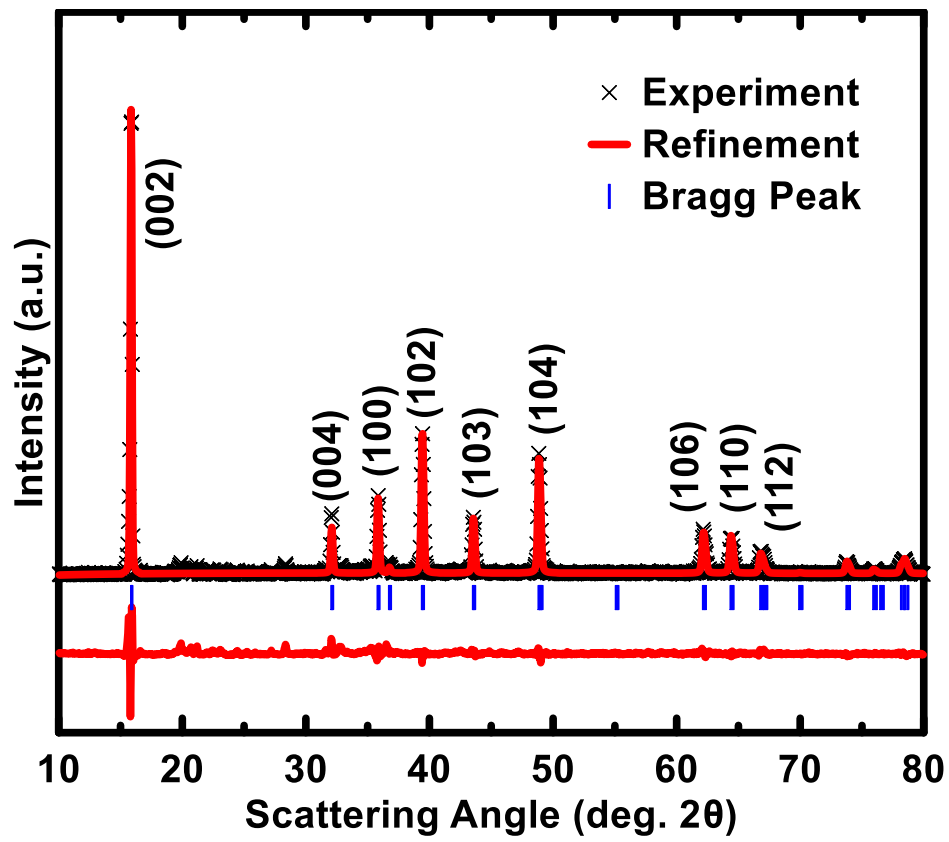


435

436

437

438 Figure 10

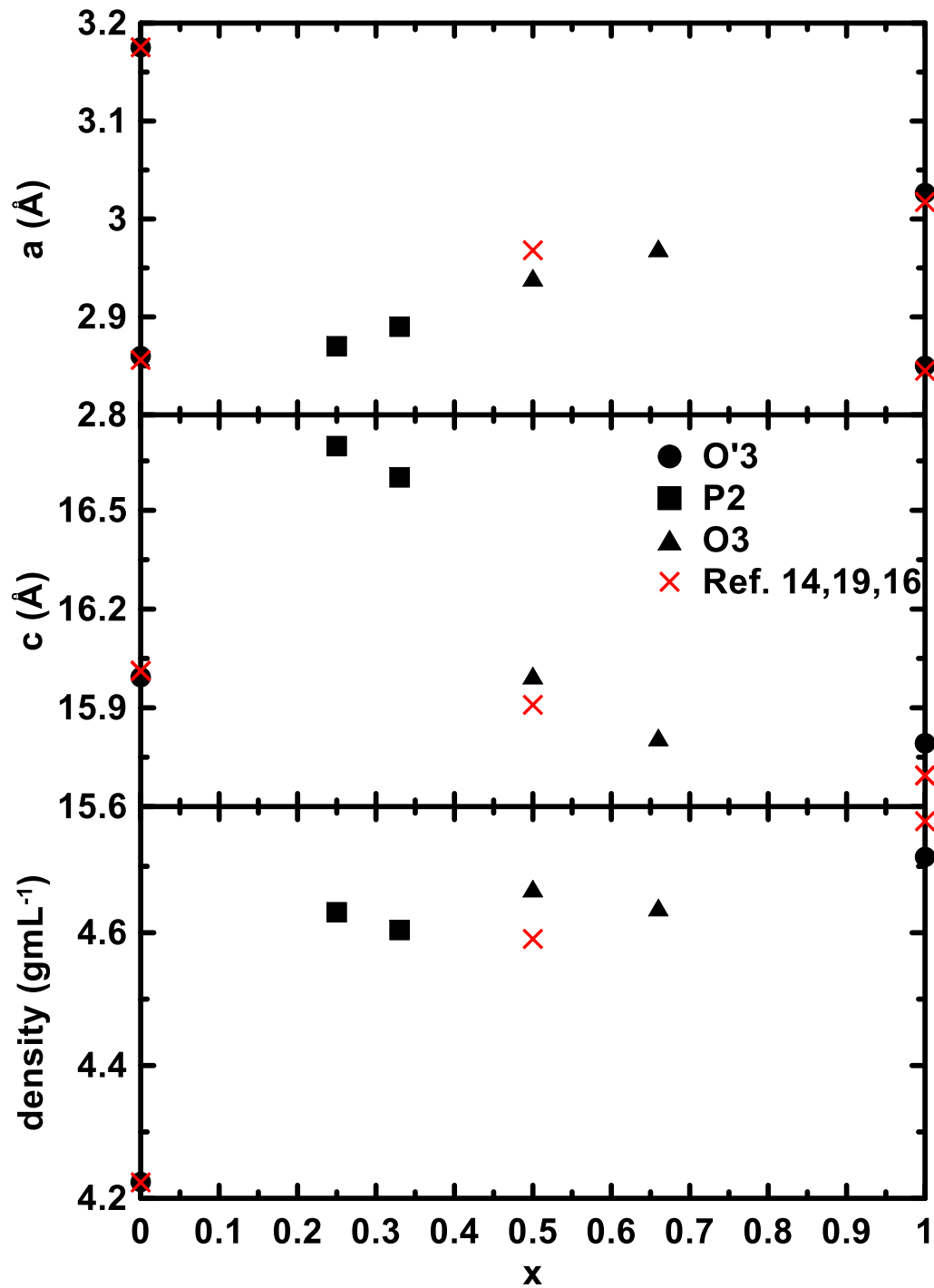


439

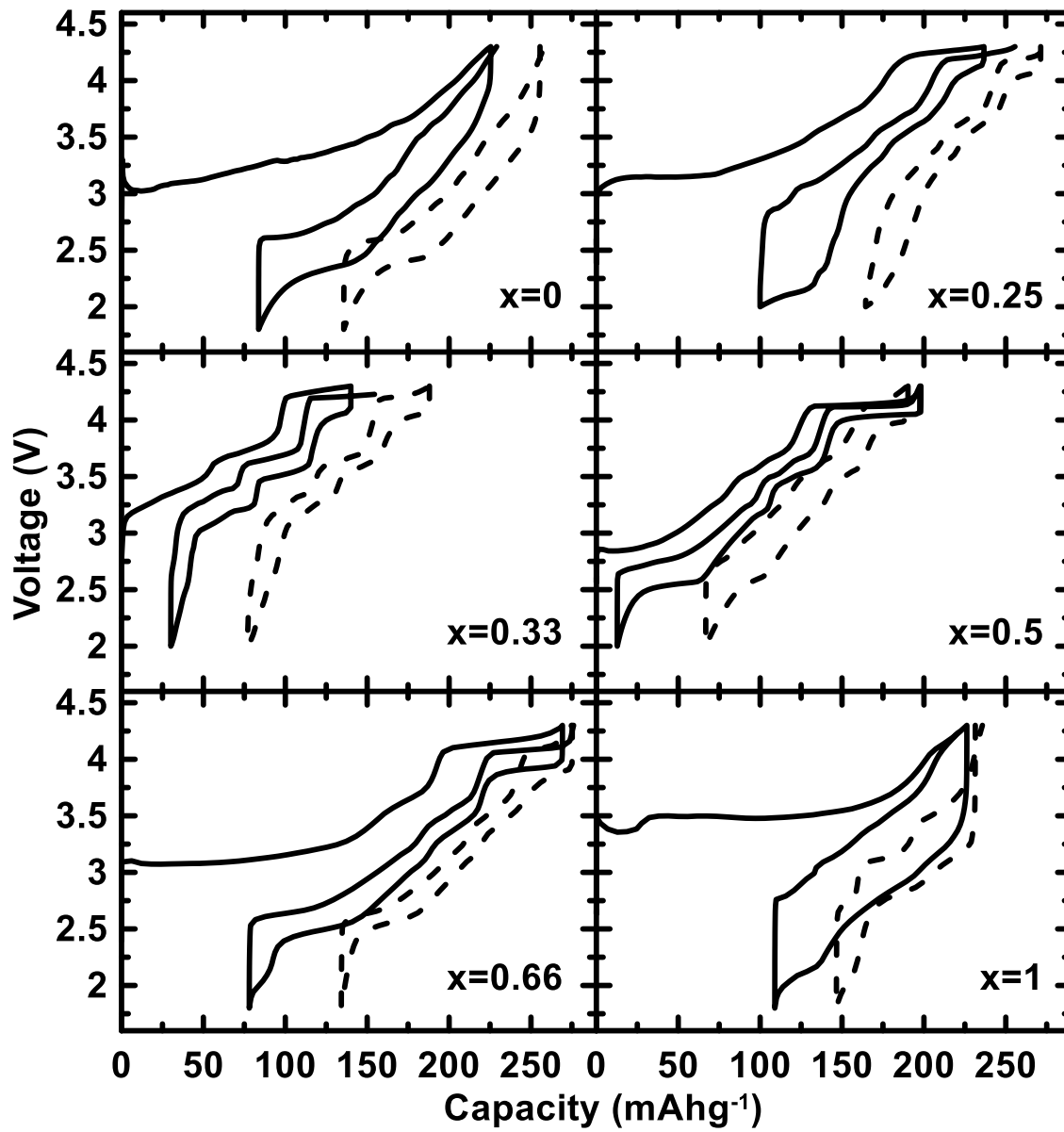
440



441 Figure 11

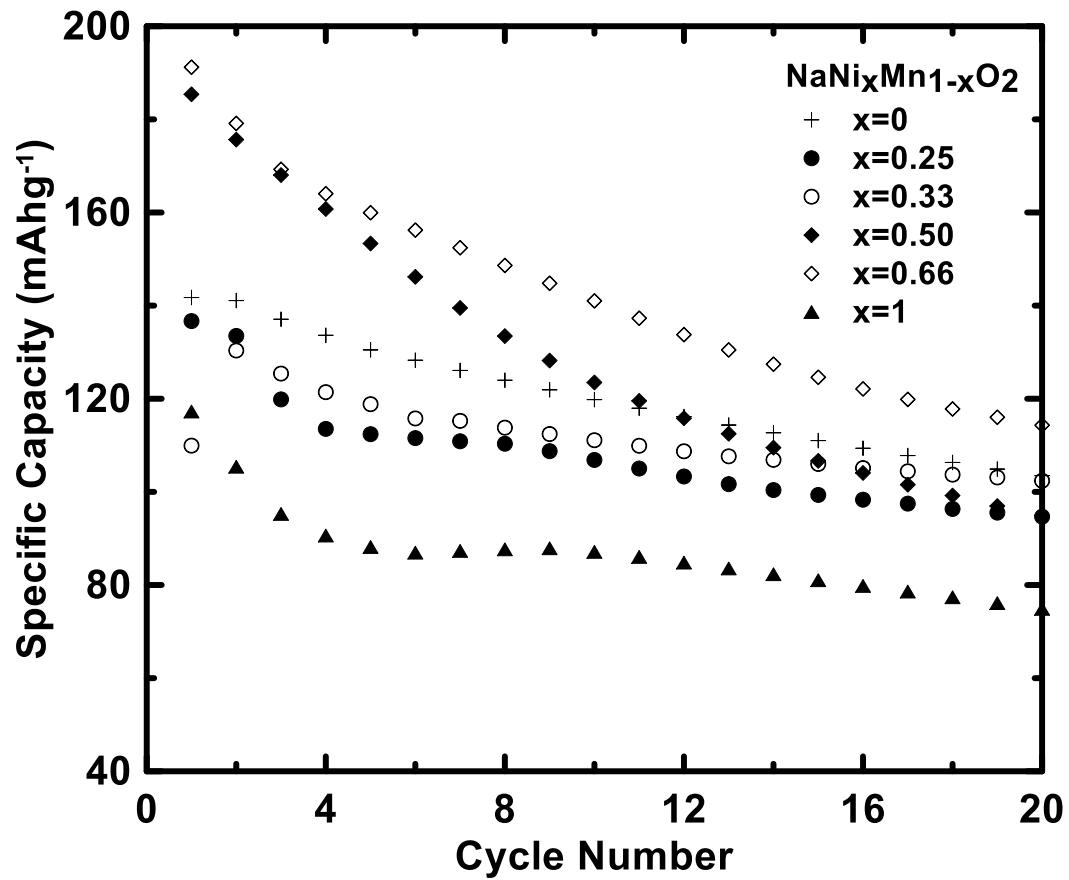


443 Figure 12



444  
445  
446

447 Figure 13



448

449

450